CrossMark

## JM RAPIDS

# Multiple lock-ins in vortex-induced vibration of a filament

Mohd Furquan[1] and Sanjay Mittal[1],†

[1]Department of Aerospace Engineering, Indian Institute of Technology Kanpur, UP 208 016, India

The vortex-induced vibration of a flexible filament attached behind a stationary cylinder is studied in the two-dimensional, laminar flow regime. We explore the response of the filament for a wide range of flexibility and inertia. Lock-in with a large number of normal modes of the filament, each in a different regime of reduced speed, is observed. Reduced speed is the free-stream speed of the incoming flow non-dimensionalized with the first natural frequency of the structure and the diameter of the cylinder. Several branches, based on response of the filament, are identified and the contributions of various structural modes along these branches are quantified. Contribution from a particular structural mode increases significantly during lock-in, accompanied by a large amplitude of vibration. The transition between different branches is found to be hysteretic and intermittent. The flow exhibits a variety of vortex-shedding patterns, including the 2P+2S mode. The modes of shedding show a systematic variation with amplitude and frequency. The map of vortex-shedding patterns in the amplitude–frequency plane resembles the corresponding map for forced vibration of a rigid cylinder. The transformation of wake from one mode of shedding to another is explained phenomenologically. Variation of rate of energy transfer between the fluid and filament with space and time is analysed to determine optimal placement of transducers for harvesting energy.

**Key words:** flow-structure interactions, vortex shedding

## 1. Introduction

A bluff body placed in a uniform stream of fluid experiences time-varying force due to shedding of vortices. Its response to this unsteady force is referred to as vortex-induced vibration (VIV). Notably, the vibration of the body can profoundly alter the flow. A remarkable feature of VIV is lock-in, wherein the body vibrates with large amplitude, over a range of reduced flow speeds, $U^*$, at close to its natural frequency. Vortex-induced vibration of a rigid circular cylinder on an elastic support, modelled by a linear

† Email address for correspondence: smittal@iitk.ac.in

spring, has been widely studied at low and high Reynolds number $Re$ (Sarpkaya 2004; Williamson & Govardhan 2004; Bearman 2011). Here, we briefly review the results for the laminar regime. Navrose & Mittal (2016) reported three types of branches in the VIV response of an isolated cylinder with $U^*$: desynchronization (DS), initial branch (IB) and lower branch (LB). The amplitude of response is very small in DS regime and the non-dimensional frequency ($F$) of vibration is close to $St_0$, the Strouhal number corresponding to vortex-shedding frequency for flow past a stationary cylinder. The lock-in regime consists of IB and LB. The cylinder undergoes high-amplitude oscillation (up to sixty per cent of its diameter) in LB that are almost sinusoidal. In IB, the power spectra of the time histories of cylinder response and the fluid force reveal two prominent peaks that are close to the natural frequency of the structure ($F_n$) and $St_0$. The flow and response is hysteretic during transition from DS to IB, IB to LB and from LB to DS; increasing- and decreasing-$U^*$ lead to different states for a certain range of $U^*$. Response frequency $F$ gets closer to $F_n$ during lock-in with increase in mass ratio $m^*$ (Navrose & Mittal 2017). The mode of vortex shedding in the laminar regime is 2S for the stationary cylinder and when the amplitude of vibration is relatively small. In this mode, two vortices of opposite sign are shed in one cycle of shedding. Larger amplitude vibration modifies the shedding to C(2S), wherein the vortices in the wake coalesce.

Splitter plates/filaments have been used in the past to control vortex shedding and the oscillations resulting from it. The earliest experimental studies were limited to the effect of rigid plates on suppressing vortex shedding (Roshko 1954, 1955; Apelt, West & Szewczyk 1973; Apelt & West 1975). Shukla, Govardhan & Arakeri (2009) observed sustained oscillations of a plate hinged behind a circular cylinder in their experiments. The oscillation amplitude showed increase with Reynolds number before attaining saturation at around $Re = 4000$. The VIV of a flexible filament attached to a bluff body is far more complex than that of rigid cylinder. Unlike the latter, the former is associated with infinite degrees of freedom, and, consequently, as many natural frequencies and their corresponding modes of vibration. In terms of its engineering applications, an optimal design of such an oscillator may be used as a passive device for either inhibiting VIV, without making the structure vulnerable to galloping (Wu *et al.* 2014; Sahu, Furquan & Mittal 2019*b*), or extracting energy from flow (Song *et al.* 2017; Soti *et al.* 2017). Despite its association with rich dynamical phenomena and its potential in practical applications, most of the past studies on vibration of a filament behind a fixed cylinder focus on its use as a benchmark problem with limited exploration of the parameter space (Wall & Ramm 1998; Turek & Hron 2006; Kalmbach & Breuer 2013). Shukla, Govardhan & Arakeri (2013) experimentally investigated the effect of Reynolds number at few values of filament stiffness. They observed two regimes of periodic oscillations with frequency close to the vortex shedding frequency of an isolated cylinder, separated by a range of aperiodic oscillations. Lee & You (2013) studied the effect of plate length at $Re = 100$. The amplitude of vibration was observed to be lowest when the length is twice the cylinder diameter. A related problem widely studied in the literature is the flutter of a flag (Zhang *et al.* 2000; Shelley & Zhang 2011). According to Shelley & Zhang (2011), the first attempt to analyse this problem was made by Rayleigh who used the Kelvin–Helmholtz-like instability to explain the flapping motion of the flag. Kelvin–Helmholtz vortices in the wake of a flapping flag were observed experimentally by Zhang *et al.* (2000). However, Argentina & Mahadevan (2005) showed that the primary mechanism driving the instability is aeroelastic flutter, while the Kelvin–Helmholtz mechanism plays a secondary role of destabilizing the vortex sheet in the wake. Several improvements have since been proposed to their model, for example, inclusion of finite

span (Eloy, Souilliez & Schouveiler 2007) and an upstream cylinder (pole) (Manela & Howe 2009). The latter study showed that vortices shed by an upstream body can trigger vibration long before the filament encounters flutter instability. The postcritical behaviour has also been studied using nonlinear beam/plate models coupled with panel methods (Tang & Paidoussis 2007) as well as the Navier–Stokes equation (Connell & Yue 2007).

In this paper, we address several questions, in the context of VIV of a flexible body, that have been earlier posed for VIV of rigid bodies: (i) What are the various branches of response and how do they relate to the natural modes of the structure? (ii) Can the response be intermittent/hysteretic? (iii) How does the flow pattern vary from one branch to another? (iv) What is the effect of mass ratio, $m^*$? (v) What is the spatio-temporal distribution of energy exchange between fluid and the structure? To the best of our knowledge there has been no organized study in the past that explores these questions. Sahu *et al.* (2019*b*) and Pfister & Marquet (2020) studied the VIV of a cylinder with a flexible plate for a limited range of $U^*$ and only one value of $m^*$. For the parameter range investigated in their study, only the first two modes were found to be relevant and only the 2S pattern of vortex shedding was reported. On the other hand, by considering a significantly larger parameter space we observe lock-in with up to fourth structural mode and a myriad of vortex-shedding patterns.

## 2. Problem description and computational details

We study the VIV of a flexible filament which is attached behind a stationary circular cylinder placed in a uniform stream. The filament models a plate of very small thickness with equivalent mass and flexural rigidity. Figure 1 shows the schematic of the set-up and the computational domain. Also shown are the conditions applied at the boundaries of the domain. The parameters relevant to VIV are $m^*$, $U^*$, $\zeta$ and $Re$. The mass ratio is defined as $m^* = \rho_s A / \rho_f D b$, where $\rho_s$ and $\rho_f$ are the respective densities of the structure and the fluid, $b$ is the span and $A$ is the cross-sectional area of the filament. Three values of $m^*$ are considered: 1, 2 and 20. The reduced speed is defined as $U^* = U/f_{n1}D$, where $f_{n1}$ is the fundamental natural frequency of the filament, $U$ is the free-stream speed of the flow and $D$ is the diameter of the cylinder. We note that the definitions of $m^*$ and $U^*$, for the flexible body, are a little different than those for the rigid body. Here $U^*$ is varied between 0 and 160. A rigid filament is represented by $U^* = 0$, while $U^* = 160$ corresponds to a filament that offers very small bending resistance. The coefficient of structural damping, $\zeta$, is fixed at zero. The Reynolds number is defined as $Re(= UD/\nu_f)$, where $\nu_f$ is the coefficient of kinematic viscosity of the fluid. Its value is 150 for this study. The flow is laminar and expected to be two-dimensional at $Re = 150$. It is, however, unsteady even for a stationary filament. The length of the filament is $L = 3.5D$, while the Poisson's ratio of its material is 0.35.

The unsteady response of the filament for different $(U^*, m^*)$ is analysed to identify the contribution of the various structural modes. Each of these modes has a distinct shape, shown in figure 2(*a*) along with their corresponding natural frequencies $F_k$, characterized by the number of nodes and anti-nodes. The displacement of the filament with respect to its undeformed geometry is zero at the nodes. For example, a filament vibrating in the first structural mode has just one node, which is at the root. Similarly, the second mode of vibration has two nodes, while the third mode has three. Let $\phi_k(X)$ be the normalized Euler–Bernoulli (EB) mode such that $\int_0^L \phi_k^2(X) \, dX = 1$. Let $Y(X, t)$ denote the vertical displacement of the filament as a function of undeformed coordinate $X$,
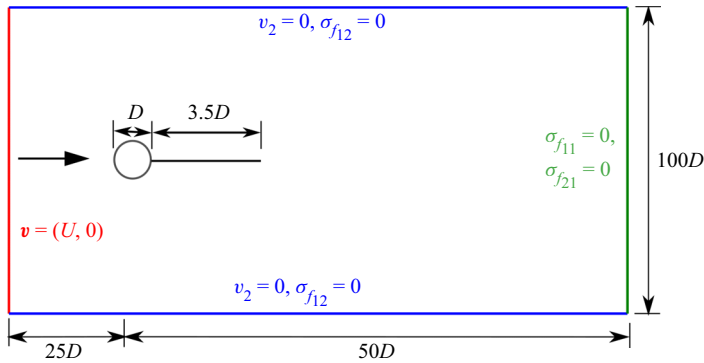
Figure 1. Schematic of the problem set-up (not to scale) for a stationary cylinder with a flexible filament. Also shown are the boundary conditions on the fluid velocity, $\boldsymbol{v}$, and the fluid stress, $\boldsymbol{\sigma}_f$. The subscripts 1 and 2 respectively denote the horizontal and vertical directions.

non-dimensionalized with $D$. The fraction of $Y(X, t)$, over $n$ complete oscillation cycles, that may be attributed to the $k$th mode $\phi_k(X)$ is estimated as

$$q_k = \frac{\int_\tau^{\tau+nT} \left( \int_0^L Y(X, t) \phi_k(X) \, \mathrm{d}X \right)^2 \mathrm{d}t}{\int_\tau^{\tau+nT} \int_0^L Y^2(X, t) \, \mathrm{d}X \, \mathrm{d}t}, \tag{2.1}$$

where $\tau$ is an arbitrary time instant and $T$ is the time period of oscillation. Similar measures have been adopted in the past as a measure of energy contribution of individual eigenmodes in flow-induced vibration of a membrane (Allen & Smits 2001) and flexible cylinder (Shang, Stone & Smits 2014).

Higher eigenmodes are excited at relatively large $U^*$ (Sahu et al. 2019b). However, numerical modelling of fluid-structure interactions becomes increasingly challenging with increase in flexibility of structures. A partitioned approach similar to Sahu et al. (2019b) has been adopted in the present work for simultaneously solving the equations governing the flow as well as the structural dynamics. The structure is modelled as a Timoshenko beam (Simo & Vu-Quoc 1986a). It is solved via Galerkin finite-element method (Simo & Vu-Quoc 1986b) and Bathe's time-integration method (Bathe 2007). A stabilized finite-element method with linear interpolation for velocity and pressure is used to model the flow (Tezduyar et al. 1992). Use of a conservative time-integration scheme and a robust model for the structure allows us to study VIV at $U^*$ that is up to an order of magnitude larger than the maximum value considered in the earlier studies (Sahu et al. 2019b; Pfister & Marquet 2020). The fluid-structure solver is validated against the benchmark problem proposed by Wall & Ramm (1998). In this set-up, a thin flexible plate of length $L = 4D$ and thickness $0.06D$, is attached to a stationary square cylinder of edge length $D$. The relatively small thickness of the plate enables modelling it as a filament with equivalent mass and flexural rigidity. The Reynolds number, based on $D$, is $Re = 332.6$. The reduced speed is $U^* = 16.94$, while the mass ratio is $m^* = 5.085$. The Poisson's ratio of the material of the filament/plate is $\nu_s = 0.35$. Table 1 lists the results from the present and past studies. The present results are in good agreement with those available in the literature.

We also compare the present results for a filament with those for a splitter plate (thickness: $0.2D$) undergoing large amplitude vibration reported by Sahu et al. (2019b). At $Re = 150$, $U^* = 80$ and $m^* = 2$, the maximum displacement of the tip of the splitter plate
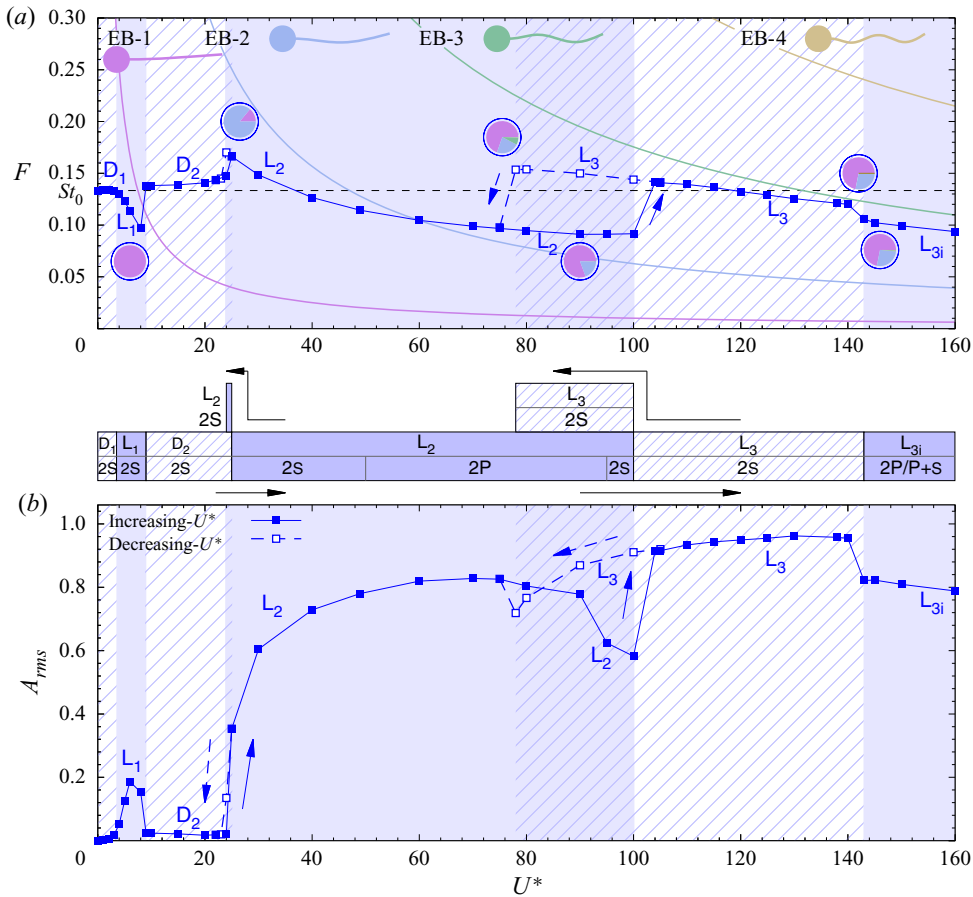
Figure 2. The $Re = 150$, $m^* = 2$ flow past a fixed cylinder with a flexible filament: variation of (*a*) dominant frequency $F$ and natural frequencies $F_k$, (*b*) r.m.s. displacement $A_{rms}$. Also shown in panel (*a*) are the contribution of various EB modes to the filament response via pie charts. The extent and layout of different branches is shown using block structures below panel (*a*) as well as by the shading of the relevant portions in panels (*a*,*b*). Letters L and D refer to lock-in and desynchronization branches. Arrows indicate the increasing- and decreasing- $U^*$ initial conditions.

| Reference | $A_{max}$ | $F$ |
|---|---|---|
| Wall & Ramm (1998) | 1.20 | 0.0604 |
| Matthies & Steindorf (2003) | 1.18 | 0.0610 |
| Bazilevs *et al.* (2008) | 1.21 | 0.0591 |
| Wood *et al.* (2008) | 1.15 | 0.0573 |
| He, Yang & Baniotopoulos (2018) | 1.24 | 0.0586 |
| Present | 1.18 | 0.0573 |

Table 1. The $Re = 332.6$ flow past a stationary square cylinder with a thin flexible plate corresponding to $U^* = 16.94$, $m^* = 5.085$: comparison of tip-displacement amplitude and frequency obtained using the present solver with the values available in the literature. $A_{max}$ denotes amplitude of tip oscillation.

| Case | NE | $\Delta t$ | $A_{rms}$ | $C_{l_{rms}}$ | $C_{d_{rms}}$ | $C_{d_{avg}}$ | F |
|------|------|-------|---------------|---------------|---------------|---------------|---------------|
| C1 | $71k$ | 0.025 | 0.7803 (1.9) | 2.2225 (1.2) | 0.6848 (0.1) | 1.7564 (2.8) | 0.1144 (1.1) |
| C2 | $174k$ | 0.025 | 0.7681 (3.4) | 2.2891 (1.7) | 0.7041 (2.7) | 1.8698 (3.5) | 0.1122 (0.9) |
| C3 | $174k$ | 0.005 | 0.7955 | 2.2502 | 0.6855 | 1.8066 | 0.1132 |

Table 2. $Re = 150$ flow past a stationary cylinder with a flexible filament corresponding to $U^* = 49$, $m^* = 2$: mesh and time-step convergence study. Here NE refers to the approximate number of elements in the mesh. Values in parenthesis are percentage deviations from the case C3; $C_l$ and $C_d$ are the lift and drag coefficients, respectively. The subscripts rms and avg refer to the r.m.s. and mean values.

is 1.206 from the present computations with a filament model, while it is 1.202 from the plate model reported by Sahu *et al.* (2019*b*). The values of frequency from the two studies are 0.095 and 0.098, respectively. The results from both the studies are in reasonable agreement. The small difference can be attributed to the difference in structural models for the splitter plate in the two studies.

Computations were carried out for VIV of flexible filament for $Re = 150$, $U^* = 49$ and $m^* = 2$ to study the adequacy of the finite-element mesh and the time step used in this study. Two meshes, with over 71 000 and 174 000 triangular elements, were considered for studying the mesh convergence. They are referred to as $71k$ and $174k$, respectively. Further, two different time steps, $\Delta t = 0.005$ and $0.025$, were used to establish time-step independence. Table 2 lists the r.m.s. of the tip displacement, $A_{rms}$, as well as the mean and r.m.s. of the force coefficient for different meshes and time steps. Also listed is the non-dimensional frequency of vibration of the plate-tip, $F$. It is seen that the maximum difference in the results from the three cases is 3.5 %. The $71k$ mesh and $\Delta t = 0.025$ are used for carrying out the computations presented in the paper.

## 3. Results and discussion

### 3.1. *Filament response: multiple lock-ins and branches*

Figure 2 shows the variation of frequency $F$ and the root mean squared amplitude $A_{rms}$ of the filament tip with $U^*$ for $m^* = 2$. The Strouhal number corresponding to the vortex-shedding frequency for a rigid filament ($St_0$) is marked in figure 2(*a*) using a broken line. The pie charts represent the fraction $q_k$ corresponding to the first few EB modes at some notable values of $U^*$ (refer to (2.1)). Also shown are the first four EB modes and variation of their corresponding non-dimensional natural frequencies $F_k$ with $U^*$. The mode shape, natural frequency and $q_k$ are depicted with the same colour for a particular mode. For example, a light-magenta colour is used for depicting the first EB mode and the quantities related to it. Similarly, the value of $q_1$ at various $(U^*, m^*)$ is displayed by the fractional area of the sector coloured light-magenta in the pie charts. The extent of various branches, in terms of $U^*$, is indicated using block structures below the frequency plot as well as with the light background shading. The blocks also indicate the type of vortex shedding observed within different branches. For example, the branch $L_2$ extends between $U^* = 25$ and 100 for increasing-$U^*$ and between 24 and 78 for decreasing-$U^*$. Further subdivison of the rectangle indicates the ranges of $U^*$ in which the 2S and the 2P vortex-shedding modes appear.

Figure 3 shows the response of a flexible filament for $m^* = 1$, 2 and 20. The format of the figure is same as figure 2. In addition, figure 3 also shows the time-averaged location
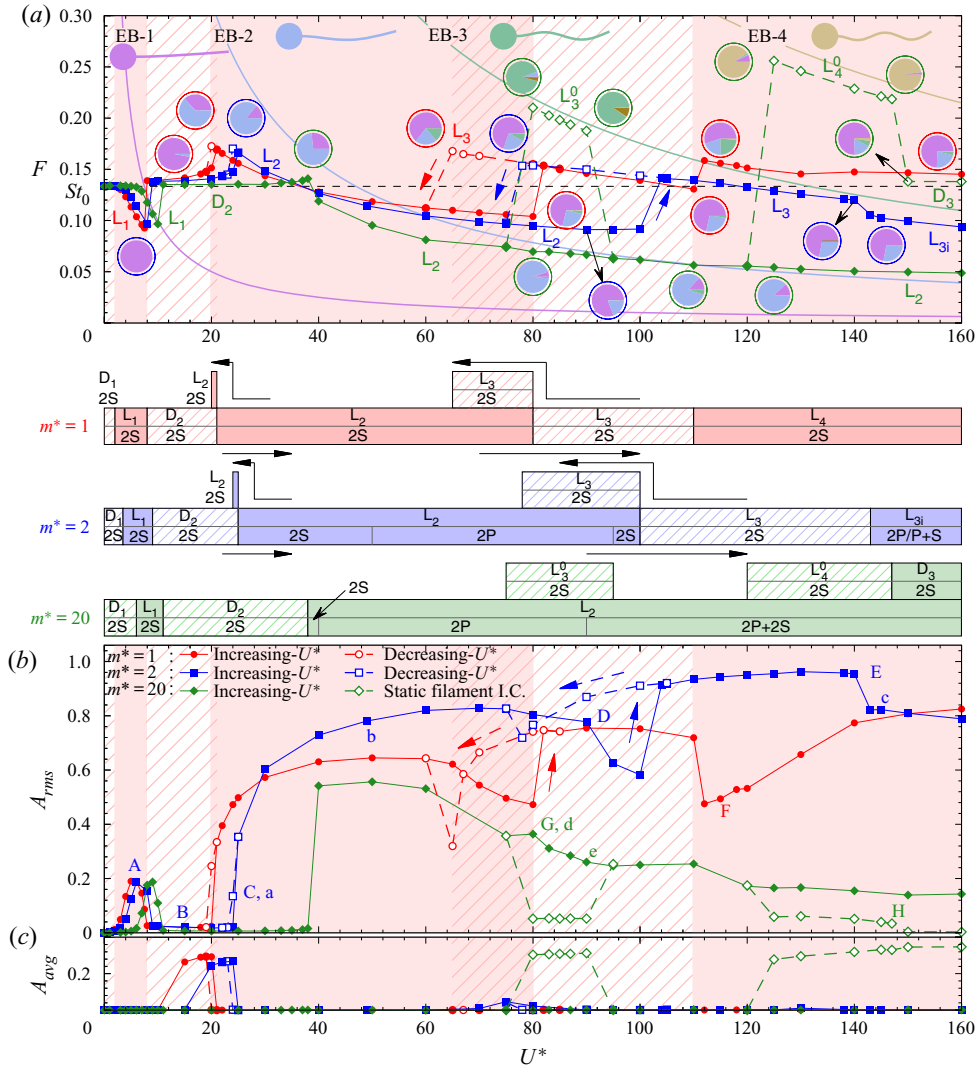
Figure 3. The $Re = 150$ flow past a fixed cylinder with a flexible filament: variation of (*a*) dominant frequency $F$ and natural frequencies $F_k$, (*b*) r.m.s. displacement $A_{rms}$ and (*c*) average displacement $A_{avg}$ of the filament tip with $U^*$ for $m^* = 1, 2$ and $20$. Pie charts in panel (*a*) show the contributions of the various EB modes. Blocks below panel (*a*) show the extent and layout of the branches. Letters L and D refer to lock-in and desynchronization branches. Arrows indicate the increasing- and decreasing-$U^*$ initial conditions.

$A_{avg}$ of the filament tip with $U^*$. The pie charts showing the contribution of various modes to filament response are enclosed in a border with colour corresponding to the relevant $m^*$. Figure 4 shows typical vorticity fields, at the time instant of maximum upward deflection, corresponding to the different vortex shedding patterns for points marked in figure 3(*b*) with letters *a* to *e*. Computations have been carried out with three initial conditions: (i) increment in $U^*$, (ii) decrement in $U^*$ and (iii) flow past stationary filament. The first two are referred to as increasing- and decreasing-$U^*$. The three initial conditions lead to the same state in most cases; the states are marked in figure 3, when they do not.
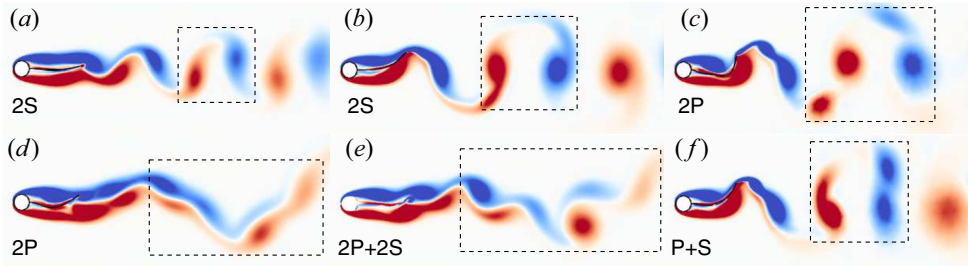
Figure 4. The $Re = 150$ flow past a fixed cylinder with a flexible filament: instantaneous vorticity fields for $(U^*, m^*) = (a)$ (24, 2), $(b)$ (49, 2), $(c,f)$ (145, 2), $(d)$ (80, 20) and $(e)$ (90, 20) when the filament tip is at its highest position. The points are indicated in figure 3$(b)$ with letters $a$ to $e$. Panels $(c)$ and $(f)$ correspond to different time instants for same point on the branch $L_{3i}$. Type of vortex shedding is also indicated. Vortices shed in one cycle are enclosed in a box.

Multiple lock-ins with different EB modes are observed. The first lock-in occurs with EB-1 on branch $L_1$, as indicated by the proximity of $F$ with $F_1$ and a peak in $A_{rms}$. The pie charts for $q_k$ confirm that the predominant mode of vibration at low $U^*$ is EB-1, and the system essentially behaves as a single degree of freedom oscillator. Branch $L_1$ is flanked on either side by the desynchronization regimes ($D_1$ and $D_2$) with relatively small $A_{rms}$ and $F$ close to $St_0$. The response of the filament in this low $U^*$ regime is qualitatively similar to the VIV of a rigid cylinder and the mode of vortex shedding is 2S.

It is found that the larger the value of $m^*$, the closer $F$ is to $F_1$ on branch $L_1$. This behaviour can be attributed to the reduction in added mass coefficient with increase in $m^*$ (Navrose & Mittal 2017). Although the peak amplitude is independent of $m^*$, it occurs at a higher $U^*$ with increase in $m^*$. These observations are consistent with VIV of rigid bodies (Sahu *et al.* 2019$a$). A notable feature of the $D_2$ branch is symmetry-breaking bifurcation, wherein the mean position of the tip is biased, for low $m^*$. A similar symmetry-breaking bifurcation has been reported in the steady solutions by Bagheri, Mazzino & Bottaro (2012). In the unsteady case, the steady bias solution serves as the base solution for the unsteady Hopf bifurcation (Pfister & Marquet 2020).

Higher modes become active at larger $U^*$ for the flexible structure. Unlike a rigid body, where further increase in $U^*$ does not bring any qualitative change in response once the second desynchronization regime sets in, the response of the flexible filament shifts from branch $D_2$ to $L_2$ with increase in $U^*$. The shift occurs via an abrupt change in the amplitude as well as frequency of oscillation. The transition between $D_2$ and $L_2$ is hysteretic, that is, the response of the system depends on increasing- vs decreasing-$U^*$. Branch $L_2$ is characterized by a significant contribution from the second, besides the first, EB mode as seen from the increase in value of $q_2$. Further, the dominant frequency of oscillations follows the $F_2$ curve. The amplitude increases significantly with increase in $U^*$ before waning off.

Branches $L_3$ and $L_4$ are characterized by significant values of $q_3$ and $q_4$. Similar to $L_2$, the onset of $L_3$ is also hysteretic. Computations initiated with flow past a stationary filament, for large $m^*$ and certain range of $U^*$, lead to branches $L_3^0$, $L_4^0$ and $D_3$. These states/branches are not approachable from $L_2$. The response on branches $L_3^0$ and $L_4^0$ are dominated by the EB-3 and EB-4 modes, respectively. However, unlike other lock-in branches, the amplitude of vibration is smaller and with a significant bias in the mean position. The effect of $m^*$ on the lock-in with EB modes is interesting. The contribution of EB-2 decreases on branch $L_2$ with increase in $U^*$ for low $m^* (= 1$ and $2)$. The behaviour of $q_3$ on branch $L_3$ is similar.

### 3.2. *Physics of vortex shedding*

Figures 3 and 4 highlight the large number of modes of vortex shedding that are observed in the free vibration of the flexible filament in the parameter space considered. Contrary to expectation, the vortex-shedding pattern is not sustained on a response branch. For example, three distinct vortex-shedding patterns are observed on $L_2$, namely 2S, 2P and 2P+2S. In general, 2S mode is observed at the lower $U^*$ end of a branch (figure 4*a*,*b*), while the more complex 2P, P+S and 2P+2S modes occur at higher $U^*$. This can be explained by looking at the variation of the vortex-shedding frequency, which is equal to $F$, over a branch. It decreases with increase in $U^*$ resulting in stretching of the shed vortices as shown in figure 4(*b*). Eventually for $F \lesssim 0.1$, the stretched vortices split into two, resulting in a transition to the 2P mode (figure 4*c*). Four vortices are shed in one cycle of 2P mode, two of the same sign from each side. A further decrease in frequency leads to an even larger stretching of vortices. When $F$ reduces to below 0.07 approximately, the stretched vortices undergo yet another split leading to a transition from the 2P to 2P+2S mode of shedding (figure 4*e*). Such low values of $F$ occur only for large $m^*$ (figure 4*e*). In the 2P+2S shedding pattern, an additional single vortex, of opposite sign, accompanies the pair of vortices seen in 2P mode (Williamson & Roshko 1988). The shedding pattern reverts back to 2S mode towards the higher $U^*$ end of $L_2$ with irregular spacing between the vortices. Unlike in VIV of rigid bodies (Mathai *et al.* 2017), the transitions between the vortex-shedding modes on the $L_2$ branch are not abrupt; rather they occur through a range of intermediate mixed states. While the mode of vortex shedding on $L_3$, $L_4$, $L_3^0$ and $L_4^0$ is 2S, intermittent switching between the 2P and P+S modes of shedding occurs on branch $L_{3i}$. Three vortices, two of the same sign, are shed in one cycle in the P+S pattern (figure 4*f*). Intermittency reduces as $U^*$ increases and eventually only the 2P mode is observed. It may be noted that the 2S mode is associated with both low and high amplitudes of vibration. However, the modes in which a larger number of vortices are shed in each cycle of oscillation appear only during lock-in when the filament vibrates with relatively large amplitude. The foregoing discussion suggests that the pattern of vortex shedding observed is largely dependent on the amplitude and frequency, irrespective of $U^*$ and the associated branch. Williamson & Roshko (1988) identified the regimes of various modes of vortex shedding for the forced vibration of a rigid cylinder on amplitude vs $St_0/F$ plane. Their experiments were conducted at relatively large $Re$. We extend their analysis to the present case of flexible filament. We replace the amplitude and frequency of forced vibration with the r.m.s. displacement and frequency of the tip of the flexible filament undergoing free vibration. The map so generated is presented in figure 5. Remarkably, it not only shows clustering of modes into distinct regions but is even qualitatively similar to the one presented in Williamson & Roshko (1988) for the rigid cylinder despite the two VIV systems being very different. This similarity may be attributed to the dependence of the vortex-shedding patterns on the wake itself and not on how the wake is generated. Figure 5 also shows that the mode shapes are relatively insignificant, compared with the tip displacement of the filament, in terms of vortex-shedding patterns. An interesting observation from figure 5 is that the extent of 2P+2S does not share a boundary with the 2S mode. Therefore, the transition from the 2S to 2P+2S mode is via 2P. We also note that both 2P and 2S modes are possible when the filament vibration frequency is less than 60 per cent of $St_0$ approximately. Which of these, 2P or 2S, is actually observed is decided by the amplitude of vibration. Unless the frequency is very low, the 2S mode is preferred for low amplitude as it is associated with a relatively narrower wake. The 2P mode results from stretching of vortices, which requires either a sufficiently low vibration frequency or a wide wake, that results from large amplitude vibration.
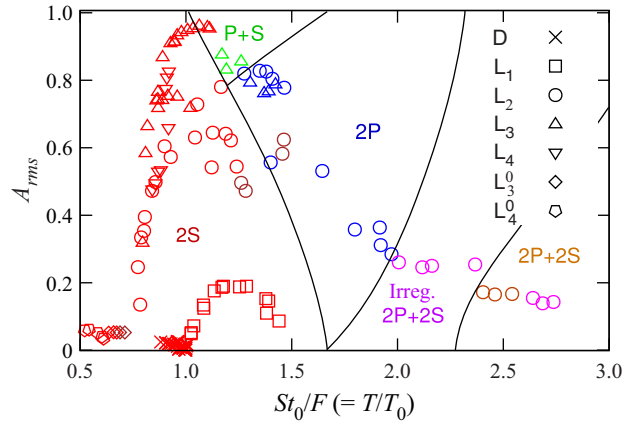
Figure 5. The $Re = 150$ flow past a fixed cylinder with a flexible filament: distribution of vortex shedding modes in the $A_{rms}$–$St_0/F$ plane for $m^* = 1, 2$ and $20$.
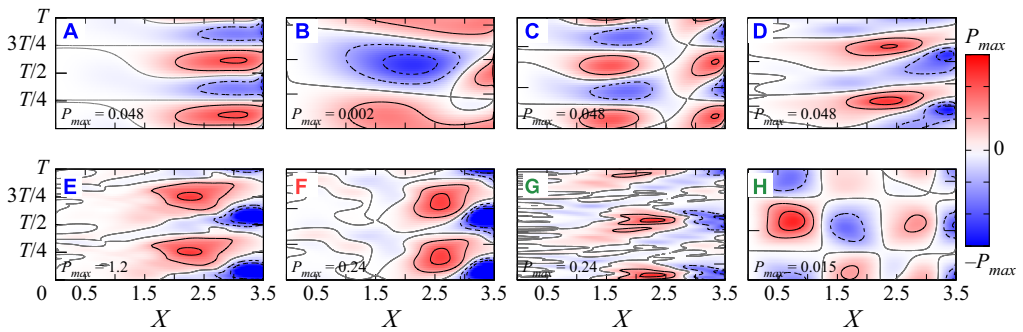


Figure 6. The $Re = 150$ flow past a fixed cylinder with a flexible filament: space–time contours showing energy (per unit length) transfer rate across the length of the filament during one cycle of oscillation at points marked using letters A to H in figure 3.

### 3.3. *Energy transfer between fluid and filament*

Kumar, Navrose & Mittal (2016) investigated the energy transfer between a rigid cylinder and fluid during VIV. Unlike a rigid body undergoing VIV, a flexible body can gain energy at one location, while simultaneously loosing some of it at another. It is, therefore, possible to locate points on the structure that absorb energy for most part of a cycle, while loosing only a small fraction of it during the remaining. This is despite the fact that no net energy is transferred to the entire structure in one complete cycle when the structural damping is zero. Popular designs for energy harvesting devices use piezo-electric or electromagnetic transducers at certain locations on the body. Identification of 'maximum energy absorption points' can be useful in the optimal placement of transducers.

Energy transfer rate (per unit length), $P(X, t)$, at a location $X$ along the filament and instant $t$ is defined as follows: $P(X, t) = v_n(X, t)[\![p(X, t)]\!]$, where $v_n(X, t)$ and $[\![p(X, t)]\!]$ respectively denote the normal component of filament velocity and difference between pressure on the two sides. The viscous forces contribute negligibly to the energy budget and are not included in the estimate. Figure 6 shows contours of $P(X, t)$ with $(X, t) \in [0, L] \times [\tau, \tau + T]$, for selected points marked with letters A to H in figure 3(*b*). A positive value of $P$ corresponds to gain in energy of the filament. The topology of the contours is

mainly governed by the underlying dominant EB mode. Cases dominated by the first EB-1 mode (A,D,E,F), show only one sink (red spot) in a half-cycle. Similarly, those dominated by the second mode (C,G) and by the fourth mode (H) respectively show two and four such spots. This pattern is consistent with the number of antinodes in the corresponding modes. Most energy contours have a period of $T/2$. However, the contours for two halves of the single cycle are different for B and H due to bias in the mean position of the filament.

As expected, maximum value of $P$ is higher when $A_{rms}$ is large (D,E,F and G). Maximum energy absorption is along $\mathsf{L}_2$, $\mathsf{L}_3$ and $\mathsf{L}_4$ branches. It is higher for $U^* \gtrsim 30$ and low $m^*$. Further, the maximum value of energy transfer rate, $P_{max}$, for most cases is located at $X \sim 2.5$–3. This, therefore, is the best location for placing transducers to extract energy. However, response of a real device will be affected by the presence of a transducer as well. The recommendations made here are suggestive, aimed towards narrowing down the already vast parameter space.

## 4. Conclusions

We have identified, by investigating a wide range of inertia and flexibility, lock-in branches corresponding to the first four EB modes in the response of a flexible filament behind a cylinder. Response of the filament shifts abruptly, and hysteretically, from one branch to another as $U^*$ is varied. Each such transition is accompanied by a sharp change in the contribution of a particular EB mode. Increasing inertia of the filament brings its frequency closer to the natural frequency during lock-in. There is no fixed vortex-shedding pattern for a branch, rather the frequency and amplitude of a state decide the type of pattern observed. While the simpler 2S pattern is observed at higher frequencies, one of the more complex 2P, P+S and 2P+2S patterns gets selected, based on the value of amplitude, at lower frequencies. Using r.m.s. amplitude and the dominant frequency of the tip vibration, we have generalized the delimitation of vortex-shedding modes in the amplitude–frequency plane from forced vibration of a cylinder (Williamson & Roshko 1988) to the present case. That the vortex-shedding map for rigid and flexible bodies have strong similarities, suggests that it might be possible to construct a universal map valid for all wakes irrespective of the geometric complexity of the body. The spatio-temporal distribution of energy transfer primarily depends on the dominant EB mode. Maximum gain in energy of the filament takes place at approximately 70 %–85 % of its length from the base and its value correlates well with the amplitude of vibration.

**Author ORCIDs.**
Sanjay Mittal https://orcid.org/0000-0002-3066-1067.

REFERENCES

ALLEN, J.J. & SMITS, A.J. 2001 Energy harvesting eel. *J. Fluids Struct.* **15**, 629–640.

APELT, C.J. & WEST, G.S. 1975 The effects of wake splitter plates on bluff-body flow in the range $10^4 < R < 5 \times 10^4$. Part 2. *J. Fluid Mech.* **71** (1), 145–160.

APELT, C.J., WEST, G.S. & SZEWCZYK, A.A. 1973 The effects of wake splitter plates on the flow past a circular cylinder in the range $10^4 < R < 5 \times 10^4$. *J. Fluid Mech.* **61** (1), 187–198.

ARGENTINA, M. & MAHADEVAN, L. 2005 Fluid-flow-induced flutter of a flag. *Proc. Natl Acad. Sci. USA* **102** (6), 1829–1834.

BAGHERI, S., MAZZINO, A & BOTTARO, A. 2012 Spontaneous symmetry breaking of a hinged flapping filament generates lift. *Phys. Rev. Lett.* **109**, 154502.

BATHE, K.J. 2007 Conserving energy and momentum in nonlinear dynamics: a simple implicit time integration scheme. *Comput. Struct.* **85**, 437–445.

BAZILEVS, Y., CALO, V.M., HUGHES, T.J.R. & ZHANG, Y. 2008 Isogeometric fluid-structure interaction: theory, algorithms, and computations. *Comput. Mech.* **43**, 3–37.

BEARMAN, P.W. 2011 Circular cylinder wakes and vortex-induced vibrations. *J. Fluids Struct.* **27** (5), 648–658.

CONNELL, B.S.H. & YUE, D.K.P. 2007 Flapping dynamics of a flag in a uniform stream. *J. Fluid Mech.* **581**, 33–67.

ELOY, C., SOUILLIEZ, C. & SCHOUVEILER, L. 2007 Flutter of a rectangular plate. *J. Fluids Struct.* **23**, 904–919.

HE, T., YANG, J. & BANIOTOPOULOS, C. 2018 Improving the CBS-based partitioned semi-implicit coupling algorithm for fluid-structure interaction. *Intl J. Numer. Meth. Fluids* **87** (9), 463–486.

KALMBACH, A. & BREUER, M. 2013 Experimental PIV/V3V measurements of vortex-induced fluid-structure interaction in turbulent flow – a new benchmark FSI-PfS-2a. *J. Fluids Struct.* **42**, 369–387.

KUMAR, S., NAVROSE & MITTAL, S. 2016 Lock-in in forced vibration of a circular cylinder. *Phys. Fluids* **28**, 113605.

LEE, J. & YOU, D. 2013 Study of vortex-shedding-induced vibration of a flexible splitter plate behind a cylinder. *Phys. Fluids* **25** (11), 110811.

MANELA, A. & HOWE, M.S. 2009 The forced motion of a flag. *J. Fluid Mech.* **635**, 439–454.

MATHAI, V., ZHU, X., SUN, C. & LOHSE, D. 2017 Mass and moment of inertia govern the transition in the dynamics and wakes of freely rising and falling cylinders. *Phys. Rev. Lett.* **119**, 054501.

MATTHIES, H.G. & STEINDORF, J. 2003 Partitioned strong coupling algorithms for fluid-structure interaction. *Comput. Struct.* **81** (8), 805–812.

NAVROSE & MITTAL, S. 2016 Lock-in in vortex-induced vibration. *J. Fluid Mech.* **794**, 565–594.

NAVROSE & MITTAL, S. 2017 The critical mass phenomenon in vortex-induced vibration at low *Re*. *J. Fluid Mech.* **820**, 159–186.

PFISTER, J.L. & MARQUET, O. 2020 Fluid-structure stability analyses and nonlinear dynamics of flexible splitter plates interacting with a circular cylinder flow. *J. Fluid Mech.* **896**, A24.

ROSHKO, A. 1954 On the drag and shedding frequency of two-dimensional bluff bodies. *NACA Tech. Rep.* 3169

ROSHKO, A. 1955 On the wake and drag of bluff bodies. *J. Aeronaut. Sci.* **22** (2), 124–132.

SAHU, T.R., FURQUAN, M., JAISWAL, Y. & MITTAL, S. 2019*a* Flow-induced vibration of a circular cylinder with rigid splitter plate. *J. Fluids Struct.* **89**, 244–256.

SAHU, T.R., FURQUAN, M. & MITTAL, S. 2019*b* Numerical study of flow-induced vibration of a circular cylinder with attached flexible splitter plate at low *Re*. *J. Fluid Mech.* **880**, 551–593.

SARPKAYA, T. 2004 A critical review of the intrinsic nature of vortex-induced vibrations. *J. Fluids Struct.* **19** (4), 389–447.

SHANG, J.K., STONE, H.A. & SMITS, A.J. 2014 Vortex and structural dynamics of a flexible cylinder in cross-flow. *Phys. Fluids* **26**, 053605.

SHELLEY, M.J. & ZHANG, J. 2011 Flapping and bending bodies interacting with fluid flows. *Annu. Rev. Fluid Mech.* **43**, 449–465.

SHUKLA, S., GOVARDHAN, R.N. & ARAKERI, J.H. 2009 Flow over a cylinder with a hinged-splitter plate. *J. Fluids Struct.* **25** (4), 713–720.

SHUKLA, S., GOVARDHAN, R.N. & ARAKERI, J.H. 2013 Dynamics of a flexible splitter plate in the wake of a circular cylinder. *J. Fluids Struct.* **41**, 127–134.

SIMO, J.C. & VU-QUOC, L. 1986*a* On the dynamics of flexible beams under large overall motions – the plane case: Part I. *J. Appl. Mech.* **53**, 849–854.

SIMO, J.C. & VU-QUOC, L. 1986*b* On the dynamics of flexible beams under large overall motions – the plane case: Part II. *J. Appl. Mech.* **53**, 855–863.

SONG, J., HU, G., TSE, K.T., LI, S.W. & KWOK, K.C.S. 2017 Performance of a circular cylinder piezoelectric wind energy harvester fitted with a splitter plate. *Appl. Phys. Lett.* **111**, 223903.

SOTI, A.K., THOMPSON, M.C., SHERIDAN, J. & BHARADWAJ, R. 2017 Harnessing electrical power from vortex-induced vibration of a circular cylinder. *J. Fluids Struct.* **70**, 360–373.

TANG, L. & PAIDOUSSIS, M.P. 2007 On the instability and the post-critical behaviour of two-dimensional cantilevered flexible plates in axial flow. *J. Sound Vib.* **305**, 97–115.

TEZDUYAR, T.E., MITTAL, S., RAY, S.E. & SHIH, R. 1992 Incompressible flow computations with stabilized bilinear and linear equal-order-interpolation velocity-pressure elements. *Comput. Meth. Appl. Mech. Engng* **9** (2), 221–242.

TUREK, S. & HRON, J. 2006 *Proposal for Numerical Benchmarking of Fluid-Structure Interaction between an Elastic Object and Laminar Incompressible Flow*, pp. 371–385. Springer.

WALL, W.A. & RAMM, E. 1998 Fluid-structure interaction based upon a stabilized (ALE) finite element method. In *4th World Congress on Computational Mechanics, CIMNE, Barcelona, Spain, Computational Mechanics: New trends and Applications* (ed. S.R. Idelsohn & E. Onate). CIMNE.

WILLIAMSON, C.H.K. & GOVARDHAN, R. 2004 Vortex-induced vibrations. *Annu. Rev. Fluid Mech.* **36**, 423–455.

WILLIAMSON, C.H.K. & ROSHKO, A. 1988 Vortex formation in the wake of an oscillating cylinder. *J. Fluids Struct.* **2**, 355–381.

WOOD, C., GIL, A.J., HASSAN, O. & BONET, J. 2008 A partitioned coupling approach for dynamic fluid-structure interaction with applications to biological membranes. *Intl J. Numer. Meth. Fluids* **57** (5), 555–581.

WU, J., QIU, Y.L., SHU, C. & ZHAO, N. 2014 Flow control of a circular cylinder by using an attached flexible filament. *Phys. Fluids* **26**, 103601.

ZHANG, J., CHILDRESS, S., LIBCHABER, A. & MICHAEL SHELLEY, M. 2000 Flexible filaments in a flowing soap film as a model for one-dimensional flags in a two-dimensional wind. *Nature* **408**, 835–839.